Received: 19 October 2022 | Revised: 25 January 2023 | Accepted: 25 January 2023

DOI: 10.1002/mrm.29616

RESEARCH ARTICLE

Magnetic Resonance in Medicine

Blood-brain barrier water exchange measurements using FEXI: Impact of modeling paradigm and relaxation time effects

Elizabeth Powell[1] | **Yolanda Ohene**[2,3] | **Marco Battiston**[4] | **Ben R. Dickie**[3,5] | **Laura M. Parkes**[2,3] | **Geoff J. M. Parker**[1,4,6]

[1]Centre for Medical Image Computing, Department of Medical Physics and Biomedical Engineering, University College London, London, UK

[2]Division of Psychology, Communication and Human Neuroscience, School of Health Sciences, Faculty of Biology, Medicine and Health, University of Manchester, Manchester, UK

[3]Geoffrey Jefferson Brain Research Centre, Manchester Academic Health Science Centre, University of Manchester, Manchester, UK

[4]Queen Square MS Centre, UCL Institute of Neurology, University College London, London, UK

[5]Division of Informatics, Imaging and Data Sciences, School of Health Sciences, Faculty of Biology, Medicine and Health, University of Manchester, Manchester, UK

[6]Bioxydyn Limited, Manchester, UK

Correspondence
Elizabeth Powell, Department of Medical Physics and Biomedical Engineering, University College London, 90 High Holborn, London WC1V 6LJ, UK.
Email: e-powell@ucl.ac.uk

Funding information
Engineering and Physical Sciences Research Council, Grant/Award Numbers: EP/M020533/1, EP/S031510/1

Purpose: To evaluate potential modeling paradigms and the impact of relaxation time effects on human blood-brain barrier (BBB) water exchange measurements using FEXI (BBB-FEXI), and to quantify the accuracy, precision, and repeatability of BBB-FEXI exchange rate estimates at 3 T.

Methods: Three modeling paradigms were evaluated: (i) the apparent exchange rate (AXR) model; (ii) a two-compartment model (2CM) explicitly representing intra- and extravascular signal components, and (iii) a two-compartment model additionally accounting for finite compartmental T_1 and T_2 relaxation times ($2CM_r$). Each model had three free parameters. Simulations quantified biases introduced by the assumption of infinite relaxation times in the AXR and 2CM models, as well as the accuracy and precision of all three models. The scan–rescan repeatability of all paradigms was quantified for the first time in vivo in 10 healthy volunteers (age range 23–52 years; five female).

Results: The assumption of infinite relaxation times yielded exchange rate errors in simulations up to 42%/14% in the AXR/2CM models, respectively. Accuracy was highest in the compartmental models; precision was best in the AXR model. Scan–rescan repeatability in vivo was good for all models, with negligible bias and repeatability coefficients in grey matter of $RC_{AXR} = 0.43\,s^{-1}$, $RC_{2CM} = 0.51\,s^{-1}$, and $RC_{2CM_r} = 0.61\,s^{-1}$.

Conclusion: Compartmental modelling of BBB-FEXI signals can provide accurate and repeatable measurements of BBB water exchange; however, relaxation time and partial volume effects may cause model-dependent biases.

KEYWORDS
blood-brain barrier, diffusion MRI, FEXI, permeability, water exchange

This is an open access article under the terms of the Creative Commons Attribution License, which permits use, distribution and reproduction in any medium, provided the original work is properly cited.
© 2023 The Authors. *Magnetic Resonance in Medicine* published by Wiley Periodicals LLC on behalf of International Society for Magnetic Resonance in Medicine.

15222594, 0, Downloaded from https://onlinelibrary.wiley.com/doi/10.1002/mrm.29616 by University College London UCL Library Services, Wiley Online Library on [21/03/2023]. See the Terms and Conditions (https://onlinelibrary.wiley.com/terms-and-conditions) on Wiley Online Library for rules of use; OA articles are governed by the applicable Creative Commons License

1 | INTRODUCTION

The blood-brain barrier (BBB) separates the vasculature from brain tissue, and is important for maintaining normal brain function. Active transport of molecules necessary for metabolism is controlled by specialized proteins sited on the luminal and abluminal endothelial membranes, with passive diffusion restricted by tight junction proteins that seal together the endothelial cells. BBB dysfunction, where damage to the barrier allows pathogens and toxins to leak from the blood into the brain, is indicated in a majority of neurodegenerative diseases[1-8] as well as in stroke,[9,10] multiple sclerosis,[11-14] psychosis,[15] brain tumors[16,17] and normal aging.[1,2,18] There is increasing evidence to suggest that BBB alterations occur early in disease, so detecting subtle changes to BBB function may provide valuable insight into pathogenesis;[2,4] however, the primary established method for detecting elevated capillary leakiness—dynamic contrast-enhanced MRI—has limited sensitivity to minor damage owing to the relatively large molecular size of the contrast agent chelate as well as signal confounds caused by a range of imaging artifacts.[5,19-22]

Measurements of water exchange across the BBB using MRI provide promising new biomarkers for identifying subtle changes in BBB function.[23] Existing techniques for measuring water exchange fall broadly into three categories: (i) relaxometry-based;[5,8,14,24] (ii) arterial spin labelling (ASL)-based,[18,25-35] and; (iii) diffusion-based.[36-38] ASL-based approaches currently dominate the available methods: contrast agents are not required, as is typical in relaxometry-based approaches, and complimentary physiological parameters such as cerebral blood flow are also extracted. However, while altered exchange rates have successfully been detected in a range of diseases,[16,27,39] ASL-based approaches are often limited by low signal-to-noise ratio (SNR), resulting in long scan times. Diffusion-based methods, which have only recently been proposed, have the potential to overcome some of these limitations.

Filtered-exchange imaging (FEXI)[40-42]—a technique originally developed to measure water exchange across cell membranes by exploiting the difference in diffusivities between tissue compartments—can be adapted to measure exchange across the BBB (here denoted BBB-FEXI).[36-38] While initial BBB-FEXI results show promise, current approaches rely on several critical assumptions and simplifications. For example, when applying FEXI to study cell membrane water exchange, biases due to intercompartmental T_1 and T_2 relaxation differences have been observed.[41,43] Relaxation time effects are inherently intertwined with exchange effects, as different rates of signal recovery and decay in different compartments will affect the observed relative signal fractions in a similar manner to exchange between compartments. Bias in BBB water exchange rate estimation is therefore to be expected if relaxation is not explicitly accounted for. While the impact of T_1 may be approximated and corrected,[41] T_2 effects are harder to compensate for.[43] This becomes of increasing importance for BBB-FEXI measurements in the presence of pathology, where tissue T_1 and T_2 often change, frequently in tandem with BBB disruption.

A second potentially significant limitation of current BBB-FEXI approaches is that compartmentalization has not been explicitly modeled. Instead, an apparent exchange rate (AXR) has been used to approximate the true water exchange rate,[36] as was introduced for cell membrane measurements using FEXI.[41,42] AXR has the potential to be biased relative to the true underlying exchange rate owing to relaxation time differences[41,43] and does not provide insight into other potentially useful biomarkers, such as blood and tissue volume fractions and diffusivities. Finally, the accuracy, precision, and repeatability of BBB-FEXI (for any modeling paradigm) has not yet been demonstrated.

The above considerations motivate the aims of this work, which are: (i) to evaluate compartmental modeling as a means of providing greater biophysical insight into BBB function; (ii) to quantify the impact of relaxation time effects on exchange rate estimation in both the compartmental and AXR models of BBB-FEXI; (iii) to evaluate the accuracy and precision of the different modeling paradigms by employing signal simulations, and (iv) to evaluate for the first time the scan–rescan repeatability of BBB-FEXI measurements in healthy subjects.

2 | THEORY

2.1 | Two-compartment exchange model

Given a two-compartment system (here describing intra- and extravascular tissue components as in Figure 1A), the general solution for the magnetization at time t, $\boldsymbol{M}(t)$, given the magnetization state at time $t = t_0$, $\boldsymbol{M}(t_0)$, and at equilibrium, $\boldsymbol{M}^{\mathrm{eq}}$, is:[44,45]

$$\boldsymbol{M}(t) - \boldsymbol{M}^{\mathrm{eq}} = e^{-\left(q^2\boldsymbol{D}+\boldsymbol{R}^{(1,2)}+\boldsymbol{K}\right)(t-t_0)}\left[\boldsymbol{M}(t_0) - \boldsymbol{M}^{\mathrm{eq}}\right], \quad (1)$$

where

$$\boldsymbol{M} = \begin{bmatrix} m_i \\ m_e \end{bmatrix}, \quad \boldsymbol{D} = \begin{bmatrix} D_i & 0 \\ 0 & D_e \end{bmatrix}, \quad \boldsymbol{R} = \begin{bmatrix} R_i & 0 \\ 0 & R_e \end{bmatrix}, \quad \text{and}$$

$$\boldsymbol{K} = \begin{bmatrix} k_{ie} & -k_{ei} \\ -k_{ie} & k_{ei} \end{bmatrix}, \quad (2)$$

15222594, 0, Downloaded from https://onlinelibrary.wiley.com/doi/10.1002/mrm.29616 by University College London UCL Library Services, Wiley Online Library on [21/03/2023]. See the Terms and Conditions (https://onlinelibrary.wiley.com/terms-and-conditions) on Wiley Online Library for rules of use; OA articles are governed by the applicable Creative Commons License

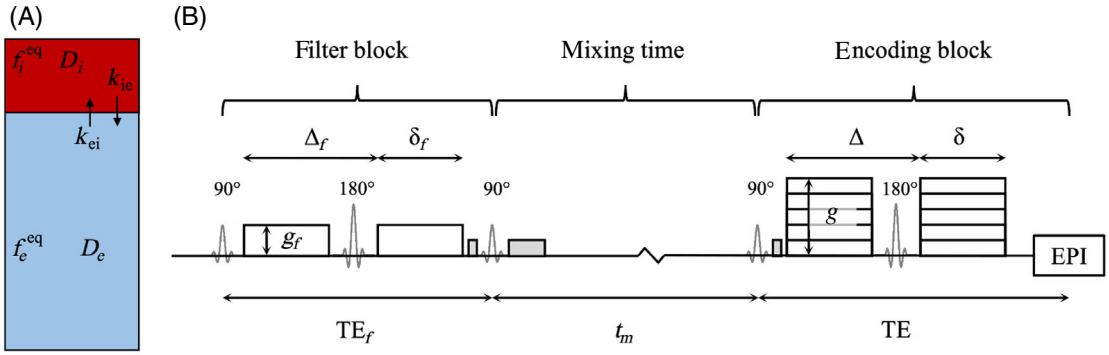

FIGURE 1 Blood-brain barrier (BBB) water exchange measurements using filtered-exchange imaging (BBB-FEXI) signal model and pulse sequence diagram. (A). The two compartment model, composed of intra- and extravascular tissue components subscripted i and e, respectively. Each compartment has an associated equilibrium signal fraction (f_i^{eq},f_e^{eq}) and diffusivity (D_i, D_e) (note this is a pseudo-diffusivity in the intravascular compartment). (B). Pulse sequence diagram. The diffusion filter block (subscripted f) and encoding block are defined by the gradient strength (g_f, g), duration (δ_f, δ), and separation (Δ_f, Δ). Dephasing gradients before and after the longitudinal magnetization storage pulses (second and third 90° pulses) and during the mixing time are shown in grey.

and subscripts i and e indicate the intra- and extravascular compartments. For longitudinal magnetization, $M_{i,e}^{eq} = M_{i,e}^0$, $R_i = 1/T_{1,i}$ and $R_e = 1/T_{1,e}$; for transverse magnetization, $M_{i,e}^{eq} = 0$, $R_i = 1/T_{2,i}$ and $R_e = 1/T_{2,e}$. The diffusion weighting is given by $b = q^2 t = (\gamma\delta G)^2 t$, where q is the dephasing magnitude, γ is the gyromagnetic ratio, δ is the duration of the diffusion encoding gradients, and G is the diffusion encoding gradient strength. The extravascular diffusivity is represented by D_e and the intravascular pseudo-diffusivity by D_i. The intravascular-to-extravascular and extravasular-to-intravascular exchange rates are denoted k_{ie} and k_{ei}, respectively. The exchange rate matrix $\boldsymbol{K}$ conserves the total magnetization such that $\boldsymbol{K}\boldsymbol{M}^{\mathbf{eq}} = 0$ and $k_{ie} = k\, m_e^{eq}$.[44]

The diffusion filter in the FEXI pulse sequence (Figure 1B) applies a low b-value to selectively suppress the signal from fast-diffusing intravascular spins. Immediately after the diffusion filter, at time $t = \mathrm{TE}_f$ after the first 90° pulse, the magnetization is:

$$\boldsymbol{M}\left(\mathrm{TE}_f\right) = \boldsymbol{M}^0 e^{-\left(q_f^2 \boldsymbol{D} + \boldsymbol{R}_2\right)\mathrm{TE}_f}, \tag{3}$$

where q_f is the dephasing magnitude of the filter gradients. During the mixing time t_m, in which the magnetization has been longitudinally stored by the second 90° pulse, exchange and T_1 relaxation govern its evolution such that at time $t = \mathrm{TE}_f + t_m$ the magnetization is:

$$\boldsymbol{M}\left(\mathrm{TE}_f + t_m\right) = \boldsymbol{M}^{eq} + \left[\boldsymbol{M}\left(\mathrm{TE}_f\right) - \boldsymbol{M}^{eq}\right] e^{-(\boldsymbol{R}_1 + \boldsymbol{K})t_m}. \tag{4}$$

Dephasing gradients before the second and after the third 90° pulses select only the coherent magnetization encoded during the filter block and remove all other echo pathways, including any inflow effects (i.e. $\boldsymbol{M}^{eq} = 0$ in Equation 4). The eigenvalues and eigenvectors used in the determination of the matrix exponential in Equation (4) are provided in Appendix A.

The detected signal, that is the magnetization after the second diffusion encoding block at time $t = \mathrm{TE}_f + t_m + \mathrm{TE}$, is:

$$\boldsymbol{M}\left(\mathrm{TE}_f + t_m + \mathrm{TE}\right)|_{q>0} = \boldsymbol{M}\left(\mathrm{TE}_f + t_m + \mathrm{TE}\right)|_{q=0}\, e^{-q^2 \boldsymbol{D}\cdot\mathrm{TE}}, \tag{5}$$

where $\boldsymbol{M}\left(\mathrm{TE}_f + t_m + \mathrm{TE}\right)|_{q=0} = \boldsymbol{M}\left(\mathrm{TE}_f + t_m\right) e^{-\boldsymbol{R}_2\cdot\mathrm{TE}}$ is the magnetization at time $t = \mathrm{TE}_f + t_m + \mathrm{TE}$ with $q = 0$.

Simplifications to Equation (5) can be made in the absence of relaxation effects. As total magnetization is now preserved, the magnetization components can be described in terms of signal fractions, where at all times $f_i + f_e = 1$. The signal after the filter block can then be described according to:

$$S\left(b_f\right) = S_0\left(\left(1 - f_i^{eq}\right) e^{-b_f D_e} + f_i^{eq} e^{-b_f D_i}\right), \tag{6}$$

where S_0 is the signal with $b_f = 0$. Immediately after the diffusion filter, the intra- and extravascular signal fractions are described by f_i^0 and f_e^0, respectively. Exchange during the mixing time leads to a recovery of the fractional populations toward their equilibrium values subject to the exchange rate $k = k_{ie} + k_{ei}$:[40]

$$f_i\left(t_m\right) = f_i^{eq} - \left(f_i^{eq} - f_i^0\right) e^{-k t_m}. \tag{7}$$

The signal measured after the encoding block in the absence of relaxation effects is then:[40]

$$S\left(b_f, t_m, b\right) = S\left(b_f, t_m\right)\left(\left(1 - f_i\left(t_m\right)\right) e^{-bD_e} + f_i\left(t_m\right) e^{-bD_i}\right), \tag{8}$$

15222594, 0, Downloaded from https://onlinelibrary.wiley.com/doi/10.1002/mrm.29616 by University College London UCL Library Services, Wiley Online Library on [21/03/2023]. See the Terms and Conditions (https://onlinelibrary.wiley.com/terms-and-conditions) on Wiley Online Library for rules of use; OA articles are governed by the applicable Creative Commons License

TABLE 1 Acquisition parameters.

	T_1w FFE	DW-EPI	BBB-FEXI			
Resolution (mm^3)	$1 \times 1 \times 1$	$3 \times 3 \times 5$	$3 \times 3 \times 5$			
Repetition time, TR (ms)	25	5000	5000			
Echo time, TE (ms)	3	62	62			
b-values (s/mm^2)	—	0, 1000	0, 50, 100, 250, 1000			
Gradient directions	—	1, 6	3, 3, 3, 3, 3			
Averages	1	6	5			
Total volumes	1	42	300			
Scan time (min, s)	4′30″	4′10″	25′40″			
Filter echo time, TE_f (ms)	—	—	38			
Filter *b*-values, b_f (s/mm^2)	—	—	0	250	250	250
Mixing time, t_m (ms)	—	—	20	20	200	400

Notes: All scans were acquired with SENSE acceleration factor 2. Total acquisition time was 36 min.
Abbreviations: BBB-FEXI, blood-brain barrier (BBB) water exchange measurements using filtered-exchange imaging .

where b is the diffusion weighting of the encoding block and $S\left(b_f, t_m\right)$ the filtered signal with $b = 0$.

2.2 | AXR model

The signal after a single diffusion experiment (i.e., Equation 6) can be approximated as:

$$S(b) = S_0\, e^{-b\cdot \mathrm{ADC}}, \tag{9}$$

where the apparent diffusion coefficient is $\mathrm{ADC} = f_e^{\mathrm{eq}} D_e + f_i^{\mathrm{eq}} D_i$. In an analogous manner, the FEXI signal can be approximated as:[41]

$$S\left(b_f, t_m, b\right) = S\left(b_f, t_m\right) e^{-b\cdot \mathrm{ADC}'(t_m)}, \tag{10}$$

where the mixing-time-dependent ADC, $\mathrm{ADC}'(t_m)$, is given by[41]

$$\mathrm{ADC}'(t_m) = \mathrm{ADC}\left(1 - \sigma e^{-t_m\cdot \mathrm{AXR}}\right), \tag{11}$$

and the filter efficiency σ is defined as[41]

$$\sigma = \frac{(D_e - D_i)\left(f_e^{\mathrm{eq}} - f_e^0\right)}{\mathrm{ADC}}. \tag{12}$$

In a two-compartment system, the AXR is equivalent to the total exchange rate: $\mathrm{AXR} = k_{ie} + k_{ei}$.

3 | METHODS

Three modeling paradigms were evaluated: (i) the AXR model (Equations 10–12), giving the apparent exchange rate denoted AXR; (ii) the two-compartment model neglecting relaxation (Equations 6–8), denoted 2CM and giving the average exchange rate denoted $k\,(= k_{ie} + k_{ei})$, and; (iii) the two-compartment model including relaxation (Equations1–5), denoted $2\mathrm{CM}_r$ and giving the average exchange rate denoted k_r. The impact of relaxation time effects was first evaluated for the AXR and 2CM models using noise-free simulations; the accuracy and precision of all three paradigms were then quantified under varying noise levels. Lastly, a repeatability study was conducted for all models in a cohort of healthy subjects.

All simulations and parameter estimations were performed in Matlab 2019b (The Mathworks). Sequence parameters for the simulation experiments were matched to the in vivo acquisitions (Table 1). Before fitting, signals were normalized using the signal at $b = 0$ (in the encoding block) with corresponding filter b-value and mixing time. Equilibrium blood signal fractions were fixed at 5% in grey matter (GM) and 3% in white matter (WM)[46-48] for the compartmental models to stabilize fitting and to maintain the same number of free parameters as the AXR model. Free parameters in the AXR model were the ADC, AXR, and filter efficiency σ; for the compartmental models they were the intra- and extravascular diffusivities, D_i and D_e, and exchange rate k (2CM) or k_r ($2\mathrm{CM}_r$). Parameters were constrained in all simulation experiments as follows: (i) $0.1\,\mu m^2/ms \le \mathrm{ADC} \le 3.5\,\mu m^2/ms$, $0 \le \sigma \le 1$ and $\mathrm{AXR} > 0\,s^{-1}$ for the AXR model; (ii) $0.1\,\mu m^2/ms \le D_e \le 3.5\,\mu m^2/ms$, $3\,\mu m^2/ms \le D_i \le 30\,\mu m^2/ms$ and $k, k_r > 0\,s^{-1}$ for the 2CM and $2\mathrm{CM}_r$ models. A table of all model assumptions is provided in Table S1.

Relaxation times in vivo at 3 T were taken as: (i) $T_{1,i} = 1.65\,s$,[49] $T_{2,i} = 0.180\,s$[50] in blood; (ii) $T_{1,e} = 0.90\,s$,[51] $T_{2,e} =$

15222594, 0, Downloaded from https://onlinelibrary.wiley.com/doi/10.1002/mrm.29616 by University College London UCL Library Services, Wiley Online Library on [21/03/2023]. See the Terms and Conditions (https://onlinelibrary.wiley.com/terms-and-conditions) on Wiley Online Library for rules of use; OA articles are governed by the applicable Creative Commons License

TABLE 2 Simulated parameter values.

	$T_{1,e}$ (s)	$T_{1,i}$ (s)	$T_{2,e}$ (s)	$T_{2,i}$ (s)	f_i^{eq} (a.u.)	k (s^{-1})
Relaxation time effects						
(i) Grey matter	0.7–2.5	0.7–2.5	∞	∞	0.05	3
(ii) Grey matter	∞	∞	0.05 – 0.20	0.05 – 0.20	0.05	3
(iii) Grey matter	0.7–2.5	1.65	∞	∞	0.05	3
(iv) Grey matter	∞	∞	0.05–0.20	0.18	0.05	3
Biases from fixed parameters						
(i) White matter	0.9	1.65	0.070	0.18	0.015–0.045	3
(i) Grey matter	1.5	1.65	0.095	0.18	0.025–0.075	3
(ii) White matter	0.77–1.04	1.65	0.070	0.18	0.03	3
(ii) Grey matter	1.28–1.73	1.65	0.095	0.18	0.05	3
(iii) White matter	0.9	1.65	0.06–0.08	0.18	0.03	3
(iii) Grey matter	1.5	1.65	0.08–0.11	0.18	0.05	3
Accuracy and precision						
(i) Grey matter	1.5	1.65	0.095	0.18	0.01–0.10	0.5–20

Notes: Ground truth generative parameter values are shown for each simulation experiment. In all cases the diffusivities of tissue and blood were $D_e = 1\,\mu m^2/ms$ and $D_i = 10\,\mu m^2/ms$, respectively. All simulations used the 2CM$_r$ model for signal generation.

0.070 s[51] in WM; (iii) $T_{1,e} = 1.50$ s,[51] $T_{2,e} = 0.095$ s[51] in GM.

3.1 | Simulations

3.1.1 | Relaxation time effects

The effect of neglecting relaxation times during parameter estimation (equivalent to assuming infinite relaxation times) was investigated for a range of finite T_1 and T_2 values independently. Ground truth signals were simulated using the 2CM$_r$ model for: (i) longitudinal relaxation times for both compartments between $0.7\,s \leq T_{1,i}, T_{1,e} \leq 2.5\,s$ with $T_{2,i} = T_{2,e} = \infty$, and; (ii) transverse relaxation times between $0.05\,s \leq T_{2,i}, T_{2,e} \leq 0.20\,s$ with $T_{1,i} = T_{1,e} = \infty$. For each experiment, 2500 parameter combinations were used. Other ground truth tissue parameters are provided in Table 2. The AXR and 2CM models (which assume infinite relaxation times) were fitted to the synthesised data and initialised using the ground truth parameters. The bias in AXR and k for each parameter combination was computed as the percent relative error between the ground truth (k_{gt}) and estimated (k_{fit}) exchange rate: error $= 100 \times \left(k_{fit} - k_{gt}\right)/k_{gt}$.

The impact of mixing time on biases arising from intercompartmental T_1 differences was then investigated for three different maximum mixing times ($t_{m,\max} = 300, 400, 500$ ms), and the impact of echo time on biases arising from intercompartmental T_2 differences was analysed for three combinations of filter and encoding echo times ($TE_f/TE = 20/40, 38/62, 60/80$ ms). All other simulation parameters are in Table 2.

3.1.2 | Biases from fixed parameters

Biases incurred by fixing f_i^{eq} during parameter estimation were assessed for the 2CM and 2CM$_r$ models; the impact of fixing relaxation times was additionally explored for the 2CM$_r$ model.

Ground truth signals were generated using the 2CM$_r$ model and a range of intravascular equilibrium signal fractions between $0.015 < f_i^{eq} < 0.045$ (WM) and $0.025 < f_i^{eq} < 0.075$ (GM). Parameter estimation was performed for each simulated signal using both the 2CM and 2CM$_r$ models with the signal fraction fixed at $f_i^{eq} = 0.03/0.05$ (WM/GM), thus assessing the effect of a ±50% error in fixed value. All other generative model parameters are provided in Table 2; T_1 and T_2 were assumed infinite for parameter estimation using the 2CM model and fixed to their ground truth values for the 2CM$_r$ model.

Ground truth signals were then generated using the 2CM$_r$ model and a range of extravascular longitudinal relaxation times between $0.77\,s < T_{1,e} < 1.04\,s$ (WM) and $1.28\,s < T_{1,e} < 1.73\,s$ (GM). Parameter estimation was performed fixing $T_{1,e} = 0.90/1.50$ s (WM/GM), reflecting an error of ±15% in fixed value. All other relaxation

15222594, 0, Downloaded from https://onlinelibrary.wiley.com/doi/10.1002/mrm.29616 by University College London UCL Library Services, Wiley Online Library on [21/03/2023]. See the Terms and Conditions (https://onlinelibrary.wiley.com/terms-and-conditions) on Wiley Online Library for rules of use; OA articles are governed by the applicable Creative Commons License

times were fixed to their ground truth values (Table 2). Finally, variability in ground truth transverse relaxation time was explored for $0.060\,\text{s} < T_{2,e} < 0.081\,\text{s}$ (WM) and $0.081\,\text{s} < T_{2,e} < 0.109\,\text{s}$ (GM) with values fixed at $T_{2,e} = 0.070/0.095\,\text{s}$ (WM/GM) during parameter estimation, again reflecting an error of ±15% in fixed values relative to the ground truth. Other relaxation times were again fixed to their ground truth values (Table 2).

All fitting was performed using a single initialisation at the ground truth parameter values.

3.1.3 | Accuracy and precision

The accuracy and precision of exchange rate estimates were evaluated under varying noise conditions for each modeling paradigm. Ground truth signals were generated using the $2CM_r$ model for 100 parameter combinations between $0.01 \leq f_i^{eq} \leq 0.10$ and $0.5\,\text{s}^{-1} \leq k_r \leq 20\,\text{s}^{-1}$. All other generative tissue parameters were invariant (Table 2). Gaussian noise was added to give 1000 noisy signals for each parameter set with SNR = 60,100 (representative of the in vivo SNR) in the equilibrium signal (i.e., with $b_f = 0\,\text{s/mm}^2$, $t_m = 20\,\text{ms}$, $b = 0\,\text{s/mm}^2$). Fitting was performed as previously described, now using 20 initial values uniformly distributed between the respective parameter bounds; initial values for the exchange rate were distributed between the ground truth value ±50%. Accuracy was defined as the percent relative error of the median fitted value and precision as the interquartile range of fitted values. Extreme exchange rate estimates—defined as $\geq 40\,\text{s}^{-1}$—were discarded from calculations.

3.2 | MRI experiments

3.2.1 | Data acquisition

Ten healthy volunteers (age range 23–52 years; five female) were each scanned twice on a 3 T Philips Ingenia CX system (Philips Healthcare) using a 32-channel head coil in accordance with local ethics guidelines. The second scan was conducted in the same session for nine of the volunteers (subjects repositioned between scans); for one volunteer their second scan was 6 weeks after the first. Whole brain diffusion-weighted imaging (DWI) and T_1-weighted images were collected for registration and segmentation purposes; an additional DWI with reversed phase-encoding was acquired without diffusion weighting for susceptibility distortion correction. Single slice BBB-FEXI data were acquired using a double diffusion encoding sequence developed in-house. All acquisition parameters are provided in Table 1. Subsets of the full BBB-FEXI acquisition were formed to create different protocols for the AXR and compartmental modeling paradigms. The AXR subset contained only data acquired with encoding $b = 0{,}250\,\text{s/mm}^2$; all five repetitions of each acquisition were used, giving 120 volumes in total. The compartmental modeling subset contained two repetitions of the data acquired with all five encoding b-values, again giving 120 volumes in total and matching the AXR dataset for total acquisition time (11 min).

3.2.2 | Data analysis

The DWI were corrected for susceptibility effects using FSL's *topup* tool.[52,53] The T_1-weighted image was registered to the DWI with $b = 0\,\text{s/mm}^2$,[54] then segmented into WM, GM, and CSF using FSL FAST.[55] The MNI template was also registered to the DWI and the deformation field used to propagate the Harvard-Oxford atlas[56] into the native space of each volunteer. Each BBB-FEXI acquisition was then registered to the DWI using their respective $b = 0\,\text{s/mm}^2$ volumes and corrected for susceptibility distortions using the previously estimated off-resonance warp field. SNR in the BBB-FEXI data was calculated using the mean and SD of the five repetitions with $b_f = 0\,\text{s/mm}^2$, $t_m = 20\,\text{ms}$, $b = 0\,\text{s/mm}^2$.

Exchange rate estimates were obtained for each modeling paradigm using the relevant data subsets. Voxel-wise fitting was performed in Matlab 2019b using the Nelder-Mead nonlinear minimization method. Parameters were constrained as follows: (i) $0.1\,\mu\text{m}^2/\text{ms} \leq \text{ADC} \leq 3.5\,\mu\text{m}^2/\text{ms}$, $0.1 \leq \sigma \leq 1.0$, $0\,\text{s}^{-1} \leq \text{AXR} \leq 12.5\,\text{s}^{-1}$ for the AXR model; (ii) $0.1\,\mu\text{m}^2/\text{ms} \leq D_e \leq 3.5\,\mu\text{m}^2/\text{ms}$, $3\,\mu\text{m}^2/\text{ms} \leq D_i \leq 30\,\mu\text{m}^2/\text{ms}$, $0\,\text{s}^{-1} \leq k, k_r \leq 12.5\,\text{s}^{-1}$ for the 2CM and $2CM_r$ models. Regional exchange rate maps were created using the median voxel-wise estimate in each atlas ROI.

Bland–Altman plots were generated to assess exchange rate bias and variability between repeat scans. The repeatability coefficient was calculated for each modeling paradigm as: $\text{RC} = 1.96\sqrt{2}\sigma_w$, with σ_w the within-subject variance.[57] This quantified the smallest significant difference that may be observed between scan and rescan estimates at the 95% confidence level. Statistically significant differences ($\alpha = 0.05$) between exchange rate estimates from different modeling paradigms were calculated using a two-sample t-test on subject-wise median WM/GM values; multiple comparisons were accounted for using the Bonferroni correction.

15222594, 0, Downloaded from https://onlinelibrary.wiley.com/doi/10.1002/mrm.29616 by University College London UCL Library Services, Wiley Online Library on [21/03/2023]. See the Terms and Conditions (https://onlinelibrary.wiley.com/terms-and-conditions) on Wiley Online Library for rules of use; OA articles are governed by the applicable Creative Commons License

4 | RESULTS

4.1 | Simulations

4.1.1 | Relaxation time effects

Figure 2A shows the bias in exchange rate estimates arising from finite compartmental relaxation times under the assumption of infinite relaxation times during model fitting. For typical blood and tissue T_1 values in vivo, errors using the AXR and 2CM models were similar at approximately 14%/1% in WM/GM, respectively. Errors from T_2 differences were high for the AXR model at 42%/28% (WM/GM); errors in the 2CM model were considerably lower at 8%/6% (WM/GM).

Reducing the echo times or maximum mixing times lowered the incurred biases (Figure 2B). For example, a reduction in echo times from $TE_f/TE = 38\,ms/62\,ms$ to $TE_f/TE = 20\,ms/40\,ms$ reduced the T_2 bias in AXR estimates by almost 40% to approximately 26%/17% (WM/GM).

4.1.2 | Biases from fixed parameters

Figure 3 quantifies the biases incurred by fixing parameters in the compartmental models during parameter estimation. Major biases were observed in the 2CM model, particularly in WM: an alteration of ±50% in underlying f_i^{eq} (relative to the value fixed during fitting) incurred biases up to 82%/33% in WM/GM k estimates respectively (Figure 3A). However, note that a ±50% error in f_i^{eq} covers the wide ranges of $0.015 < f_i^{eq} < 0.045$ for WM (where fixed $f_i^{eq} = 0.030$) and $0.025 < f_i^{eq} < 0.075$ for GM (where fixed $f_i^{eq} = 0.050$). Biases were not as severe for the $2CM_r$ model, with the same ±50% error in fixed f_i^{eq} producing a 31/22% error in WM/GM k_r estimates (Figure 3B).

Fixing relaxation times had minimal impact: an error of ±15% in fixed $T_{1,e}$ or $T_{2,e}$ relative to ground truth values induced biases in the estimated k_r under 6% (Figure 3B).

4.1.3 | Accuracy and precision

Figure 4 shows the accuracy and precision in estimated exchange rates at SNR = 60 as a function of underlying f_i^{eq} and k for each modeling paradigm. The exchange rate was underestimated for the majority of tissue parameter combinations in all modeling paradigms; however, biases were greater in the AXR model than in either the 2CM or $2CM_r$ models. Accuracy was poorest for parameter combinations with low f_i^{eq} and fast k in all modeling paradigms. Precision was also worse (interquartile range was greatest) for

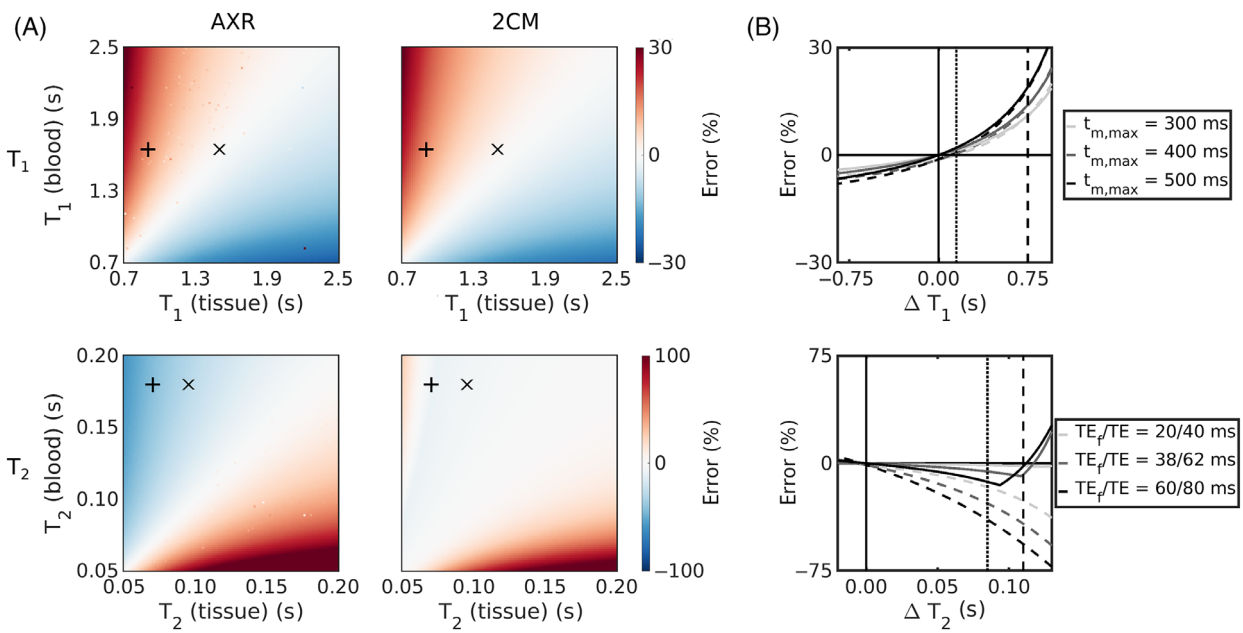

FIGURE 2 Assumption of infinite relaxation times. (A) The errors in exchange rate estimates are shown for a range of finite compartmental T_1 (top row) and T_2 (bottom row) values for the AXR (left column) and 2CM (right column) models. Expected blood/tissue values in white matter (WM) (+) and grey matter (GM) (×) are highlighted. (B) The impact of different maximum mixing times on the error in exchange rate estimates is shown for a range of T_1 differences (top); the impact of different echo times is shown for a range of T_2 differences (bottom). The AXR and 2CM models are represented by the dashed and solid lines, respectively. Expected relaxation time differences ($\Delta T = T_i - T_e$) in WM and GM in vivo are indicated by the vertical dashed and dotted lines, respectively.

15222594, 0, Downloaded from https://onlinelibrary.wiley.com/doi/10.1002/mrm.29616 by University College London UCL Library Services, Wiley Online Library on [21/03/2023]. See the Terms and Conditions (https://onlinelibrary.wiley.com/terms-and-conditions) on Wiley Online Library for rules of use; OA articles are governed by the applicable Creative Commons License

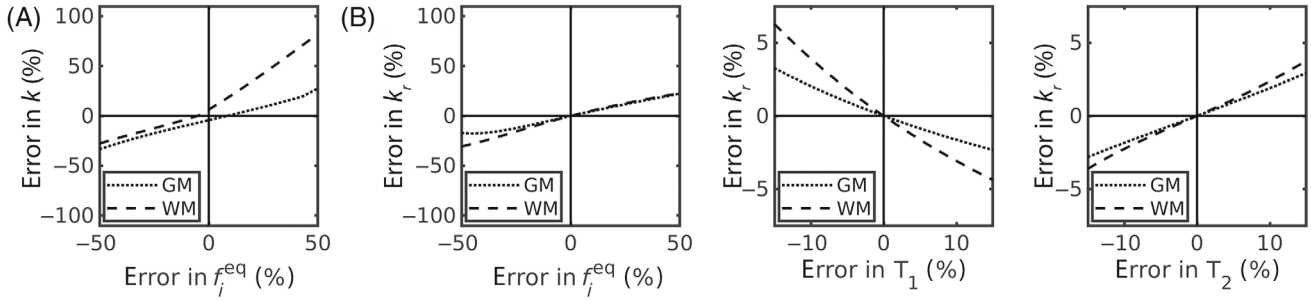

FIGURE 3 Biases in the compartmental models from fixed parameters. (A) Error in k from the 2CM model arising from errors in fixed f_i^{eq} values. (B) Error in k_r from the 2CM$_r$ model arising from errors in fixed f_i^{eq} (left), $T_{1,e}$ (center) and $T_{2,e}$ (right) values. Note that in both (A) and (B) the ±50% error in f_i^{eq} covers the approximate range $0.015 < f_i^{eq} < 0.045$ for ground truth white matter values (where fixed $f_i^{eq} \sim 0.030$) and $0.025 < f_i^{eq} < 0.075$ for ground truth grey matter values (where fixed $f_i^{eq} \sim 0.050$). Note also the change in scale for errors arising from T_1 and T_2 versus f_i^{eq}.

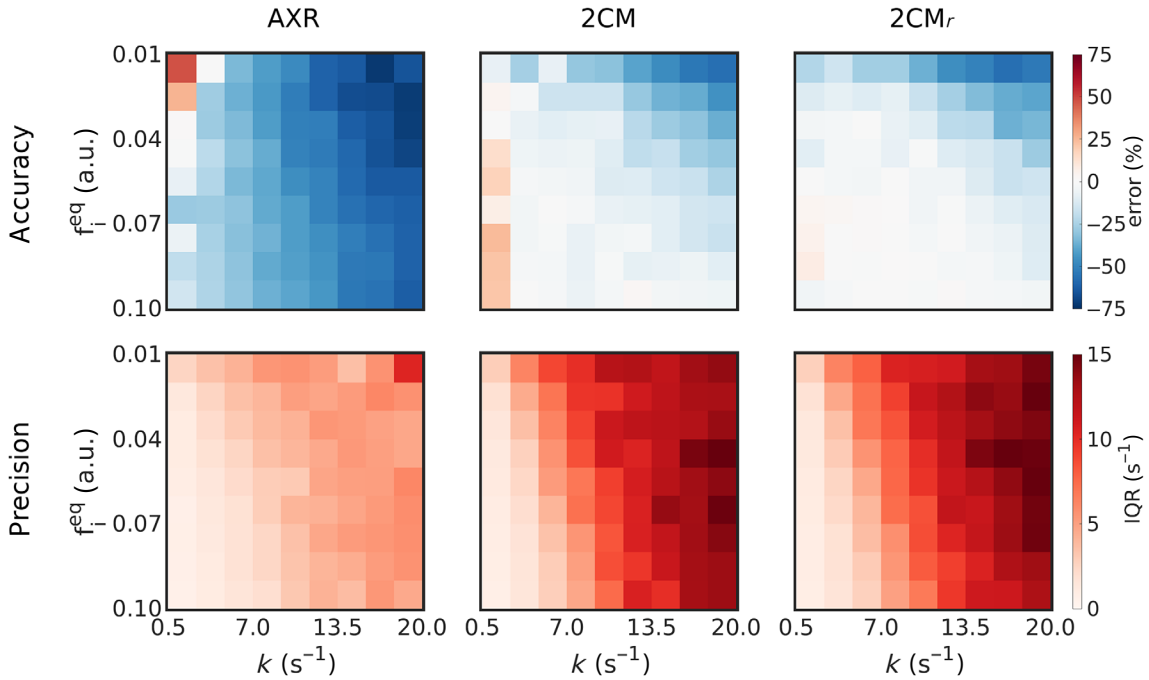

FIGURE 4 The accuracy (top row) and precision (bottom row) of estimated exchange rates are shown for a range of underlying blood volume fractions (f_i^{eq}) and exchange rates (k) for the AXR model (left column), 2CM model (centre column) and 2CM$_r$ model (right column) at SNR = 60.

the low f_i^{eq} and fast k parameter combinations, particularly for the 2CM and 2CM$_r$ models.

Figure 5 shows the distributions of all estimated parameters for three sets of tissue parameters ($f_i^{eq} = 0.05$; $k = 1.5, 3.0, 7.0\,s^{-1}$) at SNR = 100 (distributions at SNR = 60 can be found in the Figure S3). Biases were evident in all parameters of the AXR model, with the AXR and ADC notably underestimated. Most striking in the 2CM model were the distributions of D_e values, in which median values were approximately 85% greater than ground truth values. Minimal biases were observed in parameters of the 2CM$_r$ model.

4.2 | MRI experiments

Parameter maps from a representative subject are shown in Figure 6; exchange rate maps for all subjects are provided in Figure S7. Good left/right symmetry was observed for all modeling paradigms. Estimates of D_i tended toward higher values when derived from the 2CM model compared to the 2CM$_r$ model, and substantially more noise was observed in the corresponding voxel-wise fits (shown in Figure S8).

Median WM/GM parameter values are shown in Figure 7A for each subject; Table 3 provides summary

15222594, 0, Downloaded from https://onlinelibrary.wiley.com/doi/10.1002/mrm.29616 by University College London UCL Library Services, Wiley Online Library on [21/03/2023]. See the Terms and Conditions (https://onlinelibrary.wiley.com/terms-and-conditions) on Wiley Online Library for rules of use; OA articles are governed by the applicable Creative Commons License

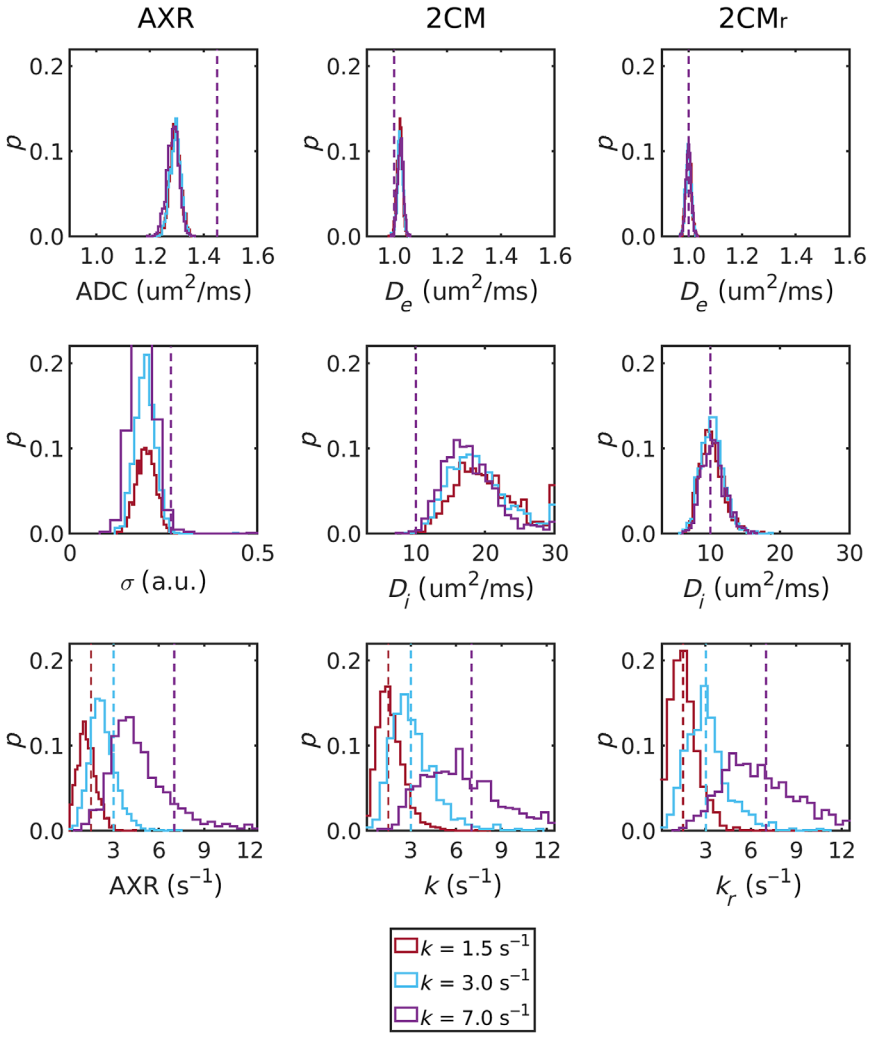

FIGURE 5 Model parameter probability distributions are shown for the AXR (left column), 2CM (center column) and $2CM_r$ (right column) models for three sets of generative parameter values ($f_i^{eq} = 0.05$; $k = 1.5, 3.0, 7.0\,s^{-1}$; SNR = 100). Ground truth (generative) values are represented by the dashed lines.

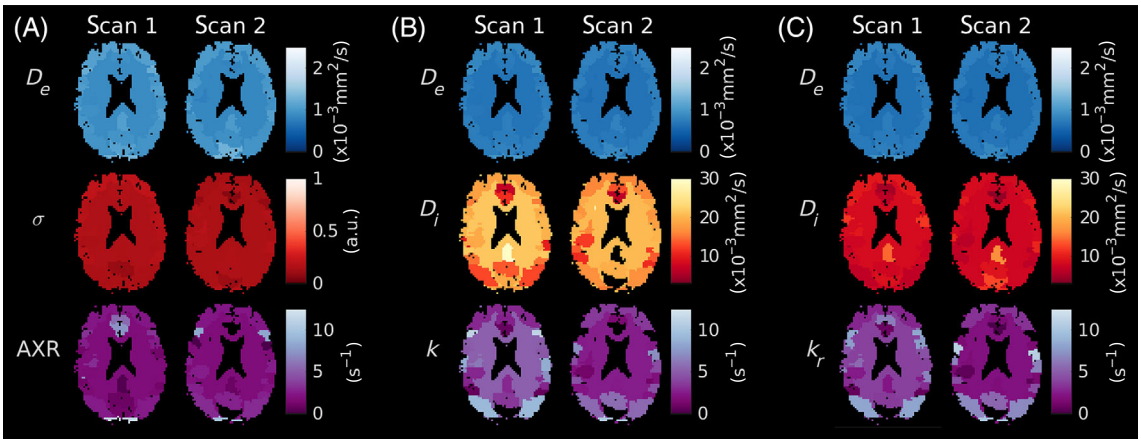

FIGURE 6 In vivo parameter maps. (A) AXR model. Parameter maps from scans 1 and 2 are shown for the ADC (top row), filter efficiency σ (middle row) and AXR (bottom row). (B) 2CM model. Parameter maps from scans 1 and 2 are shown for D_e (top row), D_i (middle row) and k (bottom row). (C) $2CM_r$ model. Parameter maps from scans 1 and 2 are shown for D_e (top row), D_i (middle row) and k_r (bottom row). All maps display the median value within each ROI; both extreme fit values and masked CSF are shown in black.

15222594, 0, Downloaded from https://onlinelibrary.wiley.com/doi/10.1002/mrm.29616 by University College London UCL Library Services, Wiley Online Library on [21/03/2023]. See the Terms and Conditions (https://onlinelibrary.wiley.com/terms-and-conditions) on Wiley Online Library for rules of use; OA articles are governed by the applicable Creative Commons License

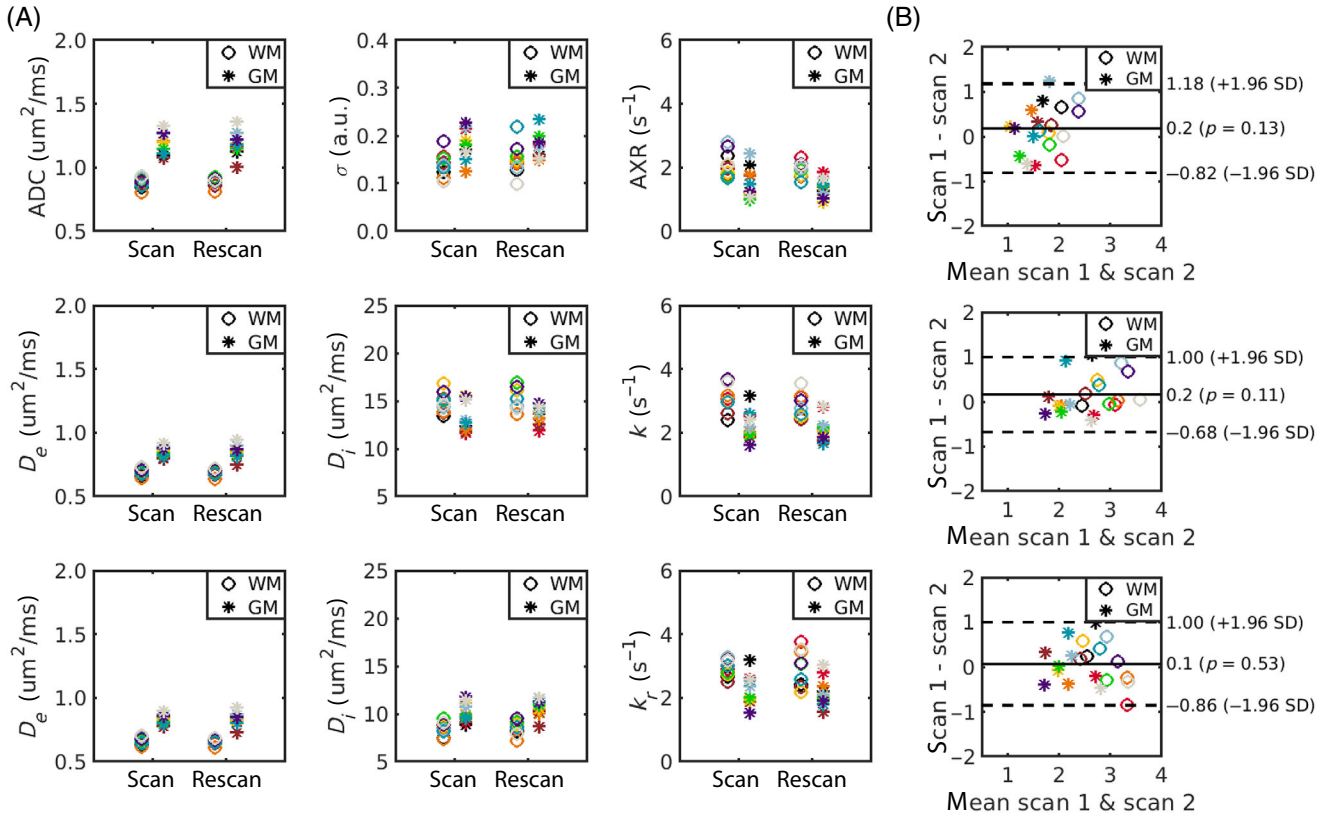

FIGURE 7 In vivo parameter comparison. (A) Median values across white matter/grey matter (WM/GM) voxels are shown for parameters from the AXR model (top row), 2CM model (middle row) and $2CM_r$ model (bottom row). (B) Bland–Altman plots for the exchange rate estimated using the AXR model (top), 2CM model (middle), and $2CM_r$ model (bottom). In all plots, each colored marker represents a single subject.

statistics over all subjects. Exchange rates in WM and GM were significantly lower when employing the AXR model than when deriving exchange rates using the 2CM and $2CM_r$ models ($p < 0.001$ for all comparisons); there were no significant differences in exchange rates between the 2CM and $2CM_r$ models ($p = 0.65/0.82$ in WM/GM). Extravascular diffusivity was higher in GM than in WM for all modeling paradigms, as defined by D_e in the compartmental models and approximated by the ADC in the AXR model. ADC values were higher than D_e for both WM and GM, reflecting the vascular contribution. The intravascular pseudo-diffusivity D_i for both WM and GM was significantly higher in the 2CM model than in the $2CM_r$ model ($p < 0.001$ for WM and GM), as observed in simulations (Figure 5).

Bland–Altman plots (Figure 7B) showed negligible bias in exchange rate measurements for all modeling paradigms; however, the 95% limits of agreement were relatively wide. The WM/GM repeatability coefficients were: $RC_{AXR} = 0.29\,s^{-1}/0.43\,s^{-1}$, $RC_{2CM} = 0.44\,s^{-1}/0.51\,s^{-1}$ and $RC_{2CM_r} = 0.52\,s^{-1}/0.61\,s^{-1}$. Repeatability coefficients for all other model parameters and the coefficients of variation can be found in Table 3.

The mean SNR in vivo was 66. An example of the acquired data can be found in Figure S5 along with a map of the fitting residuals (Figure S6).

5 | DISCUSSION

Three modeling paradigms for measuring BBB water exchange using FEXI were implemented and validated using simulations and healthy volunteers. The AXR model previously used for in vivo experiments can be hard to interpret and may not be robust to intercompartmental relaxation time differences, hence the need for a more comprehensive modeling approach; however, parameter estimation from more complex models is invariably more difficult, often resulting in better accuracy but poorer precision in the variables of interest. A more comprehensive compartmental modeling approach for quantifying BBB water exchange was proposed here, enabling for the first time explicit modeling of the blood signal component as well as consideration of relaxation time effects.

Incorporating relaxation time effects during parameter estimation was a key component of this work, as, until

15222594, 0, Downloaded from https://onlinelibrary.wiley.com/doi/10.1002/mrm.29616 by University College London UCL Library Services, Wiley Online Library on [21/03/2023]. See the Terms and Conditions (https://onlinelibrary.wiley.com/terms-and-conditions) on Wiley Online Library for rules of use; OA articles are governed by the applicable Creative Commons License

TABLE 3 Summary statistics.

		ADC ($\mu m^2/ms$)		σ (a.u.)		AXR (s^{-1})	
		WM	**GM**	**WM**	**GM**	**WM**	**GM**
AXR	Mean (SD), scan 1	0.88 (0.04)	1.19 (0.08)	0.14 (0.02)	0.18 (0.03)	2.10 (0.39)	1.53 (0.47)
	Mean (SD), scan 2	0.89 (0.03)	1.19 (0.09)	0.15 (0.03)	0.18 (0.03)	1.92 (0.23)	1.35 (0.29)
	RC	0.004	0.021	0.002	0.002	0.29	0.43
	CoV (%)	4.21	7.39	19.5	16.2	16.3	29.2
		D_e ($\mu m^2/ms$)		D_i ($\mu m^2/ms$)		k (s^{-1})	
		WM	**GM**	**WM**	**GM**	**WM**	**GM**
2CM	Mean (SD), scan 1	0.69 (0.03)	0.85 (0.04)	14.8 (1.0)	13.3 (1.5)	3.11 (0.43)	2.23 (0.46)
	Mean (SD), scan 2	0.69 (0.02)	0.85 (0.05)	15.1 (1.1)	13.6 (0.9)	2.86 (0.37)	2.16 (0.40)
	RC	0.002	0.006	3.14	4.32	0.44	0.51
	CoV (%)	3.60	5.50	7.18	9.31	13.4	20.4
		D_e ($\mu m^2/ms$)		D_i ($\mu m^2/ms$)		k_r (s^{-1})	
		WM	**GM**	**WM**	**GM**	**WM**	**GM**
$2CM_r$	Mean (SD), scan 1	0.66 (0.03)	0.83 (0.04)	8.42 (0.69)	10.2 (1.0)	2.95 (0.27)	2.27 (0.49)
	Mean (SD), scan 2	0.66 (0.02)	0.83 (0.05)	8.43 (0.68)	10.7 (0.9)	2.90 (0.55)	2.18 (0.45)
	RC	0.002	0.006	1.29	2.55	0.52	0.61
	CoV (%)	3.71	5.58	8.06	9.14	14.7	22.7

Notes: The mean and SD of median voxel-wise parameter values across subjects is shown for all modeling paradigms for scans 1 and 2, along with the repeatability coefficients (RC) and coefficients of variation (CoV).
Abbreviations: GM, grey matter; WM, white matter.

now, assuming infinite relaxation times for both compartments has been the convention in applications of FEXI for BBB water exchange measurements.[36,58] Figure 2A shows that for hypothetical substrates with the same relaxation time in both compartments this assumption can be valid, as exchange rate estimates will be minimally biased. However, for the blood and tissue relaxation times expected in vivo, this assumption introduced errors in both the AXR and 2CM models.

The largest errors due to realistic relaxation times were observed in the AXR model, and arose primarily from intercompartmental T_2 differences. The greater impact of T_2 differences (relative to T_1 differences) can be attributed in part to the combined contribution of the filter and encoding blocks compounding errors and in part to the larger difference between blood and tissue T_2 values, particularly for WM. Shortening the TE of both filter and encoding blocks was shown in simulations to reduce T_2-associated errors (Figure 2B), signifying that MRI systems with enhanced gradient characteristics—which can achieve the same diffusion weighting with a shorter TE[59]—may provide a means of alleviating T_2-associated errors in future. The superior accuracy of the 2CM model relative to the AXR model when considering relaxation time effects (Figure 2) was driven by fixing f_i^{eq}; as demonstrated in Figure S2, the reduced model stability caused by additionally estimating f_i^{eq} during model fitting generated biases comparable to those from the AXR model.

Fixing parameters, a technique widely discussed in the signal modeling community,[60,61] can however elicit unintended ramifications. Simulations in this work demonstrated that errors in fixed f_i^{eq} values could indeed induce major biases in estimated exchange rates (Figure 3), although this assumed relatively large errors up to ±50%. In this study of healthy volunteers, where inter-subject variability in blood volume was not expected, it was considered appropriate to fix f_i^{eq} in the compartmental models. However, in any future studies of clinical disorders that have associated blood volume changes,[7,62] alternative approaches may be needed. If required, this effect could be negated by providing an independent measure of blood volume. Indeed, an independent measure of blood volume would be beneficial for all modeling paradigms (including the AXR model) in order to convert the average exchange rate derived using this technique into the exchange rate from blood to tissue (often denoted k_{in}) to

15222594, 0, Downloaded from https://onlinelibrary.wiley.com/doi/10.1002/mrm.29616 by University College London UCL Library Services, Wiley Online Library on [21/03/2023]. See the Terms and Conditions (https://onlinelibrary.wiley.com/terms-and-conditions) on Wiley Online Library for rules of use; OA articles are governed by the applicable Creative Commons License

allow for more direct comparisons with other imaging techniques.

The implications of parameter fixing were also considered for the $2CM_r$ model, which, in the absence of T_1 and T_2 mapping sequences in the MRI protocol of this study, additionally required relaxation times to be fixed. By explicitly modeling finite relaxation times, the $2CM_r$ model was less affected by errors in the fixed f_i^{eq}, and, perhaps predictably, errors in fixed finite relaxation times demonstrated a comparatively low impact on parameter accuracy compared to assuming infinite relaxation times (Figure 3B). This is an important finding because relaxation times, particularly in blood, are not well defined: literature values for $T_{1,b}$ have been reported between 1.58 and 1.93 s[49,63,64] and for $T_{2,b}$ between 0.055 and 0.275 s,[50,63,65] with differences indicated between males and females, between venous and arterial blood,[64] and along the vascular tree. However, oxygenation-dependent T_2 variations[86,87] along the vasculature may be largely mitigated in using a mean T_2 value under the assumption that each large voxel contains a distribution of all vessel types (see Figure S9). Despite these uncertainties, the results here highlight the value in explicitly modeling relaxation times.

In all modeling paradigms, accuracy and precision were lowest for low f_i^{eq} values and fast exchange rates. Fast exchange rates will generally need shorter mixing times than those used in simulations here: for example, at $k = 20\,\mathrm{s}^{-1}$ the residence time is $\tau = 1/k = 50$ ms, meaning that at the simulated mixing times of $t_m = 200{,}400$ ms the intravascular component was largely recovered and little discernible difference between the two signals remained. There is also minimal perturbation of the signal by the filter block at very low f_i^{eq}, rendering the SNR used in simulations insufficient for accurate quantification of exchange rates. For expected blood volumes in vivo and at exchange rates reflective of the subtle BBB disruption the method is intended to target, distributions of fitted exchange rates (Figure 5) demonstrated that good accuracy and reasonable precision can be expected at clinically feasible SNR levels.

Distributions of D_i estimates from the 2CM model (Figure 5) revealed poor accuracy and precision, notably worse than from the $2CM_r$ model. One interpretation is that D_i captured the majority of biases arising from the infinite relaxation time assumption in the 2CM model, thus also explaining the relative lack of bias in k estimates. Post hoc analysis of the dependence of D_i estimates on relaxation times supported this theory (see Figure S4), further highlighting the value in modeling relaxation times in the $2CM_r$ model. Corresponding behaviour was observed in the in vivo data (Figure 6), and, while D_i estimates from both models were in line with previously reported values between 2 and 15 $\mu m^2/ms$,[66-68] the improved visual clarity and lower noise observed in voxel-wise D_i maps from the $2CM_r$ model (Figure S8) offered confidence that the lower values generated by this model were also more accurate. This finding may have implications beyond the current study, such as in intravoxel incoherent motion (IVIM) experiments where the assumption of infinite relaxation times in blood and tissue may similarly influence results.

Exchange rate estimates in vivo derived from each modeling paradigm also reflected the behaviors observed in simulations: there was good consistency between k and k_r, while the AXR was significantly lower (Figure 7 and Table 3). While it could be speculated that relaxation time effects caused the discrepancy between the AXR and k,k_r values (as in simulations), the in vivo condition is invariably more complex to interpret, and other factors such as additional exchanging compartments cannot be ruled out for contributing to this finding. The "true" BBB water exchange rate is also unclear: previous studies have reported values for k_{ie} in GM in the range $0.63 - 4.71\,\mathrm{s}^{-1}$.[24-27,30,36,69] Possibly the closest comparison may be made with the exchange rates reported by Bai et al.,[36] who used the FEXI approach to determine the BBB AXR. They found average values across seven subjects of AXR = $3.35\,\mathrm{s}^{-1}$ in WM and AXR = $4.71\,\mathrm{s}^{-1}$ in GM. While the findings are comparable, Bai et al.[36] report higher AXR values in GM than WM where the opposite was observed in this study (for all modeling paradigms). To date, there is considerable inconsistency in the literature, with some studies supporting the findings here[24,25,69] and others reporting trends similar to Bai et al.[26,27,36] Efforts to resolve all of these uncertainties in the field are urgently required if measurements of water exchange are to be considered as reliable biomarkers of BBB function.

All modeling paradigms showed good repeatability and negligible bias in exchange rate measurements between scans (Figure 7B). The repeatability coefficients reported here suggest that the smallest intra-subject change that can be interpreted to be a true change at the 95% confidence is approximately $\pm 0.6\,\mathrm{s}^{-1}$ for the compartmental models; this is even lower for the AXR model at $\pm 0.4\,\mathrm{s}^{-1}$, owing to its greater precision. These findings provide confidence that the BBB-FEXI method could be used to detect subtle damage.

The most appropriate of the three modeling paradigms explored in this work is likely to depend on the context of use. If relaxation time differences or changes are not expected in the chosen study populations then the AXR model may be the prudent choice: exchange rate estimates may be inaccurate, but the bias will be consistent across all subjects and the superior precision (relative to the compartmental models) may enable more subtle changes in exchange rate to be detected. However, there is evidence for relaxation time alterations in many

15222594, 0, Downloaded from https://onlinelibrary.wiley.com/doi/10.1002/mrm.29616 by University College London UCL Library Services, Wiley Online Library on [21/03/2023]. See the Terms and Conditions (https://onlinelibrary.wiley.com/terms-and-conditions) on Wiley Online Library for rules of use; OA articles are governed by the applicable Creative Commons License

neurological disorders—including dementia,[70] multiple sclerosis[71-73] and small vessel disease[74-76]—as well as in normal aging;[77-79] in these cases, simultaneous alterations in relaxation times and exchange rates may lead to unexpected results if using the AXR model. The $2CM_r$ model may then be the more robust choice, although mapping of tissue $T_{1,e}$ and $T_{2,e}$ times on an individual level may be necessary instead of relying on the literature values. Blood relaxation times taken from the literature may still be a reliable choice though, as changes are less likely unless hematocrit levels are altered as, for example, in sickle cell disease.[80] Alternatively, if blood pseudo-diffusivity is not a critical parameter for the study, then the 2CM model may also be appropriate and would bypass the requirement for relaxation time mapping, assuming that relaxation time biases continue to influence only D_i and not k; however, this warrants further validation. Overall, we anticipate that all BBB-FEXI modeling paradigms will be well suited for detecting subtle changes during early disease stages, thus providing critical information on pathogenesis. Moreover, the acquisition can be conducted in a clinically feasible time: although single-slice data were acquired here, it is possible to achieve whole-brain coverage in a comparable time owing to the long repetition time.

A limitation of the compartmental models is the need to fix f_i^{eq}; as this is a parameter liable to change in pathology, the ability to map it would be desirable. Moreover, owing to the low image resolution of the current protocol, it is possible that partial volume effects between WM and GM may introduce biases owing to incorrect assumptions regarding f_i^{eq}; however simulations (not shown) indicate that biases under 15% are expected in voxel-wise estimates, with propagation into the regional parameter estimates subsequently low. Sequence optimisation in future work could improve precision and reduce degeneracy in the model fit, subsequently enabling f_i^{eq} to be left as a free parameter during fitting. Alternatively, an independent measurement of blood volume—such as vascular space occupancy[81]—could be introduced into the imaging protocol to provide this information. The definition of blood volume itself—as the sum of arterial, venous and capillary contributions—is a limitation of all modeling paradigms: because nonpermeable arteries do not contribute to the exchange-weighted signal, exchange rates may be biased as the recovered intravascular signal will not include the arterial contribution (although exchanged spins will be present in the veins). Estimated exchange rates will therefore be lower than expected at long mixing times given the actual exchange rate, with underestimations up to 60% possible (see Section S10). This is a limitation of any BBB work utilizing the FEXI method, and is an important consideration when comparing results to the literature estimates using alternative methods.

A central assumption throughout this work was that the chosen sequence parameters rendered the signal sensitive to exchange between two compartments only, taken to be the intra- and extravascular compartments; however, the components of the BBB that were classified as intravascular were not specifically defined. While sensitivity to cellular exchange in brain tissues is unlikely for the filter b-value used here,[36,42] it is possible that exchange between perivascular CSF and interstitial water via aquaporin-4 (AQP4) located on astrocyte endfeet[82,83] may contribute to the measured water exchange rates. However, presumably the high density of AQP4 water channels covering endfeet and the large area of astocyte endfeet covering capillaries ensures that these membranes are not rate limiting for healthy brain tissues.[84] If correct, then it may not matter whether the perivascular and astrocyte structures are considered as part of the intra- or extravascular compartment. A possible exception may occur if perivascular water has a substantially different T_2 to blood or tissue. Furthermore, in pathologies where the endothelial tight junctions are damaged, astrocyte endfeet may pose a more significant barrier to water exchange, particularly if AQP4 polarization is altered or AQP4 levels are downregulated.[85] In this case, these membranes may become rate limiting. Nevertheless, this is a potentially interesting direction for future water exchange research.

6 | CONCLUSIONS

The impact of relaxation time effects, the repeatability and the clinical feasibility of three biophysical models of BBB water exchange applied to FEXI-style acquisitions were evaluated. Relaxation time effects—which are intrinsically entwined with exchange effects—can introduce substantial biases into exchange rate estimates; this was particularly evident in the AXR model. The two-compartment models, which are a step toward more comprehensive modeling of BBB exchange mechanisms, were more robust to relaxation time biases. The healthy volunteer repeatability of BBB exchange rate estimates, evaluated here for the first time, demonstrates that the BBB-FEXI technique offers a reliable approach for detecting subtle changes in BBB integrity clinically.

ACKNOWLEDGMENTS

Thanks to Dr Torben Schneider, Dr David Higgins and Dr Matthew Clemence of Philips Healthcare MR Clinical Science for their support of this work. Thanks to Dr Markus Nilsson and Dr Maxime Van Landeghem for useful discussions. Thanks to the UK MS Society and the UCL-UCLH Biomedical Research Centre for ongoing support. This work was supported by EPSRC grants

15222594, 0, Downloaded from https://onlinelibrary.wiley.com/doi/10.1002/mrm.29616 by University College London UCL Library Services, Wiley Online Library on [21/03/2023]. See the Terms and Conditions (https://onlinelibrary.wiley.com/terms-and-conditions) on Wiley Online Library for rules of use; OA articles are governed by the applicable Creative Commons License

EP/S031510/1 and EP/M020533/1; Marco Battiston was supported by the UK Multiple Sclerosis Society grant number 77/2017.

ORCID

Elizabeth Powell https://orcid.org/0000-0002-1059-1188
Marco Battiston https://orcid.org/0000-0003-2231-2251
Laura M. Parkes https://orcid.org/0000-0001-6488-507X
Geoff J. M. Parker https://orcid.org/0000-0003-2934-2234

REFERENCES

1. Farrall AJ, Wardlaw JM. Blood-brain barrier: ageing and microvascular disease - systematic review and meta-analysis. *Neurobiol Aging*. 2009;30:337-352. doi:10.1002/mrm.10640
2. Montagne A, Barnes SR, Sweeney MD, et al. Blood-brain barrier breakdown in the aging human hippocampus. *Neuron*. 2015;85:296-302. doi:10.1016/j.neuron.2014.12.032
3. van de Haar HJ, Burgmans S, Jansen JFA, et al. Blood-brain barrier leakage in patients with early Alzheimer disease. *Radiology*. 2016;281:527-535. doi:10.1148/radiol.2016152244
4. Sweeney MD, Sagare AP, Zlokovic BV. Blood-brain barrier breakdown in Alzheimer disease and other neurodegenerative disorders. *Nat Rev Neurol*. 2018;14:133-150. doi:10.1038/nrneurol.2017.188
5. Dickie BR, Vandesquille M, Ulloa J, Boutin H, Parkes LM, Parker GJ. Water-exchange MRI detects subtle blood-brain barrier breakdown in Alzheimer's disease rats. *Neuroimage*. 2019;184:349-358. doi:10.1016/j.neuroimage.2018.09.030
6. Nation DA, Sweeney MD, Montagne A, et al. Blood-brain barrier breakdown is an early biomarker of human cognitive dysfunction. *Nat Med*. 2019;25:270-276. doi:10.1038/s41591-018-0297-y
7. Al-Bachari S, Naish JH, Parker GJ, Emsley HC, Parkes LM. Blood-brain barrier leakage is increased in Parkinson's disease. *Front Physiol*. 2020;11:1-12. doi:10.3389/fphys.2020.593026
8. Dickie BR, Boutin H, Parker GJ, Parkes LM. Alzheimer's disease pathology is associated with earlier alterations to blood-brain barrier water permeability compared with healthy ageing in TgF344-AD rats. *NMR Biomed*. 2021;34:1-11. doi:10.1002/nbm.4510
9. Kim Y, Tejima E, Huang S, et al. In vivo quantification of transvascular water exchange during the acute phase of permanent stroke. *Magn Reson Med*. 2008;60:813-821. doi:10.1002/mrm.21708
10. Villringer K, Sanz Cuesta BE, Ostwaldt AC, et al. DCE-MRI blood-brain barrier assessment in acute ischemic stroke. *Neurology*. 2017;88:433-440. doi:10.1212/WNL.0000000000003566
11. Brück W, Bitsch A, Kolenda H, Brück Y, Stiefel M, Lassmann H. Inflammatory central nervous system demyelination: correlation of magnetic resonance imaging findings with lesion pathology. *Ann Neurol*. 1997;42:783-793. doi:10.1002/ana.410420515
12. Vos CMP, Geurts JJG, Montagne L, et al. Blood-brain barrier alterations in both focal and diffuse abnormalities on postmortem MRI in multiple sclerosis. *Neurobiol Dis*. 2005;20:953-960. doi:10.1016/j.nbd.2005.06.012
13. Wengler K, Ha J, Syritsyna O, et al. Abnormal blood-brain barrier water exchange in chronic multiple sclerosis lesions: a preliminary study. *Magn Reson Imaging*. 2020;70:126-133. doi:10.1016/j.mri.2020.04.017
14. Tagge IJ, Anderson VC, Springer CS, et al. Gray matter blood-brain barrier water exchange dynamics are reduced in progressive multiple sclerosis. *J Neuroimaging*. 2021;31:1111-1118. doi:10.1111/jon.12912
15. Pollak TA, Drndarski S, Stone JM, David AS, McGuire P, Abbott NJ. The blood-brain barrier in psychosis. *Lancet Psychiatry*. 2018;5:79-92. doi:10.1016/S2215-0366(17)30293-6
16. Wang J, Fernández-Seara MA, Wang S, St Lawrence KS. When perfusion meets diffusion: In vivo measurement of water permeability in human brain. *J Cereb Blood Flow Metab*. 2007;27:839-849. doi:10.1038/sj.jcbfm.9600398
17. Bai R, Wang B, Jia Y, et al. Shutter-speed DCE-MRI analyses of human glioblastoma multiforme (GBM) data. *J Magn Reson Imaging*. 2020;52:850-863. doi:10.1002/jmri.27118
18. Ohene Y, Harrison IF, Evans PG, Thomas DL, Lythgoe MF, Wells JA. Increased blood-brain barrier permeability to water in the aging brain detected using noninvasive multi-TE ASL MRI. *Magn Reson Med*. 2021;85:326-333. doi:10.1002/mrm.28496
19. Barnes SR, Ng TSC, Montagne A, Law M, Zlokovic BV, Jacobs RE. Optimal acquisition and modeling parameters for accurate assessment of low K trans blood-brain barrier permeability using dynamic contrast-enhanced MRI. *Magn Reson Med*. 2016;75:1967-1977. doi:10.1002/mrm.25793
20. Armitage PA, Farrall AJ, Carpenter TK, Doubal FN, Wardlaw JM. Use of dynamic contrast-enhanced MRI to measure subtle blood-brain barrier abnormalities. *Magn Reson Imaging*. 2011;29:305-314. doi:10.1016/j.mri.2010.09.002
21. Heye AK, Thrippleton MJ, Armitage PA, et al. Tracer kinetic modelling for DCE-MRI quantification of subtle blood-brain barrier permeability. *Neuroimage*. 2016;125:446-455. doi:10.1016/j.neuroimage.2015.10.018
22. Manning C, Stringer M, Dickie B, et al. Sources of systematic error in DCE-MRI estimation of low-level blood-brain barrier leakage. *Magn Reson Med*. 2021;86:1888-1903. doi:10.1002/mrm.28833
23. Dickie BR, Parker GJ, Parkes LM. Measuring water exchange across the blood-brain barrier using MRI. *Prog Nucl Magn Reson Spectrosc*. 2020;116:19-39. doi:10.1016/j.pnmrs.2019.09.002
24. Rooney WD, Li X, Sammi MK, Bourdette DN, Neuwelt EA, Springer CS. Mapping human brain capillary water lifetime: high-resolution metabolic neuroimaging. *NMR Biomed*. 2015;28:607-623. doi:10.1002/nbm.3294
25. St Lawrence KS, Owen D, Wang DJ. A two-stage approach for measuring vascular water exchange and arterial transit time by diffusion-weighted perfusion MRI. *Magn Reson Med*. 2012;67:1275-1284. doi:10.1002/mrm.23104
26. Wengler K, Bangiyev L, Canli T, Duong TQ, Schweitzer ME, He X. 3D MRI of whole-brain water permeability with intrinsic diffusivity encoding of arterial labeled spin (IDEALS). *Neuroimage*. 2019;189:401-414. doi:10.1016/j.neuroimage.2019.01.035
27. Shao X, Ma SJ, Casey M, D'Orazio L, Ringman JM, Wang DJ. Mapping water exchange across the blood-brain barrier using 3D diffusion-prepared arterial spin labeled perfusion MRI. *Magn Reson Med*. 2019;81:3065-3079. doi:10.1002/mrm.27632
28. Gregori J, Schuff N, Kern R, Günther M. T2-based arterial spin labeling measurements of blood to tissue water transfer in

15222594, 0, Downloaded from https://onlinelibrary.wiley.com/doi/10.1002/mrm.29616 by University College London UCL Library Services, Wiley Online Library on [21/03/2023]. See the Terms and Conditions (https://onlinelibrary.wiley.com/terms-and-conditions) on Wiley Online Library for rules of use; OA articles are governed by the applicable Creative Commons License

human brain. *J Magn Reson*. 2013;37:332-342. doi:10.1002/jmri.23822
29. Wells JA, Siow B, Lythgoe MF, Thomas DL. Measuring biexponential transverse relaxation of the ASL signal at 9.4 T to estimate arterial oxygen saturation and the time of exchange of labeled blood water into cortical brain tissue. *J Cereb Blood Flow Metab*. 2013;33:215-224. doi:10.1038/jcbfm.2012.156
30. Ohene Y, Harrison IF, Nahavandi P, et al. Non-invasive MRI of brain clearance pathways using multiple echo time arterial spin labelling: an aquaporin-4 study. *Neuroimage*. 2019;188:515-523. doi:10.1016/j.neuroimage.2018.12.026
31. Schidlowski M, Boland M, Rüber T, Stöcker T. Blood-brain barrier permeability measurement by bi-exponentially modeling whole-brain arterial spin labeling data with multiple T2-weightings. *NMR Biomed*. 2020;33:e4374. doi:10.1002/nbm.4374
32. Lin Z, Li Y, Su P, et al. Non-contrast MR imaging of blood-brain barrier permeability to water. *Magn Reson Med*. 2018;80:1507-1520. doi:10.1002/mrm.27141
33. Lin Z, Jiang D, Liu D, et al. Noncontrast assessment of blood-brain barrier permeability to water: shorter acquisition, test-retest reproducibility, and comparison with contrast-based method. *Magn Reson Med*. 2021;86:143-156. doi:10.1002/mrm.28687
34. Mahroo A, Buck MA, Huber J, et al. Robust multi-TE ASL-based blood-brain barrier integrity measurements. *Front Neurosci*. 2021;15:1-14. doi:10.3389/fnins.2021.719676
35. Lin Z, Jiang D, Liu P, Ge Y, Moghekar A, Lu H. Blood-brain barrier permeability in response to caffeine challenge. *Magn Reson Med*. 2022;88:2259-2266. doi:10.1002/mrm.29355
36. Bai R, Li Z, Sun C, Yc H, Liang H, Basser P. Feasibility of filter-exchange imaging (FEXI) in measuring different exchange processes in human brain. *Neuroimage*. 2020;219:117039. doi:10.1016/j.neuroimage.2020.117039
37. Powell E, Battiston M, Parker GJ. Diffusion-filtered exchange measurements of blood-brain barrier permeability to water. Paper presented at: Proceedings of the 29th Annual Meeting of ISMRM; 2021:1092.
38. Powell E, Ohene Y, Battiston M, Parkes LM, Parker GJ. Voxel-wise compartmental modelling of blood-brain barrier water exchange measurements using FEXI. Paper presented at: Proceedings of the 30th Annual Meeting of ISMRM, London, UK; 2022:0753.
39. Gold BT, Shao X, Sudduth TL, et al. Water exchange rate across the blood-brain barrier is associated with CSF amyloid-β 42 in healthy older adults. *Alzheimers Dement*. 2021;17:2020-2029. doi:10.1002/alz.12357
40. Åslund I, Nowacka A, Nilsson M, Topgaard D. Filter-exchange PGSE NMR determination of cell membrane permeability. *J Magn Reson*. 2009;200:291-295. doi:10.1016/j.jmr.2009.07.015
41. Lasič S, Nilsson M, Lätt J, Ståhlberg F, Topgaard D. Apparent exchange rate mapping with diffusion MRI. *Magn Reson Med*. 2011;66:356-365. doi:10.1002/mrm.22782
42. Nilsson M, Lätt J, Van Westen D, et al. Noninvasive mapping of water diffusional exchange in the human brain using filter-exchange imaging. *Magn Reson Med*. 2013;69:1573-1581. doi:10.1002/mrm.24395
43. Eriksson S, Elbing K, Söderman O, Lindkvist-Petersson K, Topgaard D, Lasič S. NMR quantification of diffusional exchange in cell suspensions with relaxation rate differences between intra and extracellular compartments. *PLoS One*. 2017;12:1-18. doi:10.1371/journal.pone.0177273
44. Van Landeghem M, Haber A, D'espinose De Lacaillerie JB, Blümich B. Analysis of multisite 2D relaxation exchange NMR. *Concepts Magn Reson Pt A*. 2010;36A:153-169. doi:10.1002/cmr.a.20157
45. Lasič S, Lundell H, Topgaard D, Dyrby TB. Effects of imaging gradients in sequences with varying longitudinal storage time-Case of diffusion exchange imaging. *Magn Reson Med*. 2018;79:2228-2235. doi:10.1002/mrm.26856
46. Yamaguchi T, Kanno I, Uemura K, et al. Reduction in regional cerebral metabolic rate of oxygen during human aging. *Stroke*. 1986;17:1220-1228. doi:10.1161/01.STR.17.6.1220
47. Leenders KL, Perani D, Lammertsma AA, et al. Cerebral blood flow, blood volume and oxygen utilization: normal values and effect of age. *Brain*. 1990;113:27-47. doi:10.1093/brain/113.1.27
48. Hatazawa J, Fujita H, Kanno I, et al. Regional cerebral blood flow, blood volume, oxygen extraction fraction, and oxygen utilization rate in normal volunteers measured by the autoradiographic technique and the single breath inhalation method. *Ann Nucl Med*. 1995;9:15-21. doi:10.1007/BF03165003
49. Lu H, Clingman C, Golay X, Van Zijl PC. Determining the longitudinal relaxation time (T1) of blood at 3.0 tesla. *Magn Reson Med*. 2004;52:679-682. doi:10.1002/mrm.20178
50. Chen JJ, Pike GB. Human whole blood T2 relaxometry at 3 tesla. *Magn Reson Med*. 2009;61:249-254. doi:10.1002/mrm.21858
51. Bojorquez JZ, Bricq S, Acquitter C, Brunotte F, Walker PM, Lalande A. What are normal relaxation times of tissues at 3 T? *Magn Reson Imaging*. 2017;35:69-80. doi:10.1016/j.mri.2016.08.021
52. Andersson J, Skare S, Ashburner J. How to correct susceptibility distortions in spin-echo echo-planar images: application to diffusion tensor imaging. *Neuroimage*. 2003;20:870-888. doi:10.1016/S1053-8119(03)00336-7
53. Smith S, Jenkinson M, Woolrich M, et al. Advances in functional and structural MR image analysis and implementation as FSL. *Neuroimage*. 2004;23:208-219. doi:10.1016/j.neuroimage.2004.07.051
54. Jenkinson M, Bannister P, Brady M, Smith S. Improved optimization for the robust and accurate linear registration and motion correction of brain images. *Neuroimage*. 2002;17:825-841. doi:10.1006/nimg.2002.1132
55. Zhang Y, Brady M, Smith S. Segmentation of brain MR images through a hidden Markov random field model and the expectation-maximization algorithm. *IEEE Trans Med Imaging*. 2001;20:45-57.
56. Desikan RS, Ségonne F, Fischl B, et al. An automated labeling system for subdividing the human cerebral cortex on MRI scans into gyral based regions of interest. *Neuroimage*. 2006;31:968-980. doi:10.1016/j.neuroimage.2006.01.021
57. Raunig DL, McShane LM, Pennello G, et al. Quantitative imaging biomarkers: a review of statistical methods for technical performance assessment. *Stat Methods Med Res*. 2015;24:27-67. doi:10.1177/0962280214537344
58. Ohene Y, Powell E, Lasič S, Parker GJ, Parkes LM, Dickie BR. Implementation of non-invasive filter-exchange imaging (FEXI) to measure blood-brain barrier water exchange in the rat brain. Paper presented at: Proceedings of the 30th Annual Meeting of ISMRM, London, UK; 2022:1217.

15222594, 0, Downloaded from https://onlinelibrary.wiley.com/doi/10.1002/mrm.29616 by University College London UCL Library Services, Wiley Online Library on [21/03/2023]. See the Terms and Conditions (https://onlinelibrary.wiley.com/terms-and-conditions) on Wiley Online Library for rules of use; OA articles are governed by the applicable Creative Commons License

59. Jones DK, Alexander DC, Bowtell R, et al. Microstructural imaging of the human brain with a 'super-scanner': 10 key advantages of ultra-strong gradients for diffusion MRI. *Neuroimage*. 2018;182:8-38. doi:10.1016/j.neuroimage.2018.05.047
60. Jelescu IO, Veraart J, Fieremans E, Novikov DS. Degeneracy in model parameter estimation for multi-compartmental diffusion in neuronal tissue. *NMR Biomed*. 2016;29:33-47. doi:10.1002/nbm.3450
61. Novikov DS, Kiselev VG, Jespersen SN. On modeling. *Magn Reson Med*. 2018;79:3172-3193. doi:10.1002/mrm.27101
62. Broom KA, Anthony DC, Blamire AM, et al. MRI reveals that early changes in cerebral blood volume precede blood-brain barrier breakdown and overt pathology in MS-like lesions in rat brain. *J Cereb Blood Flow Metab*. 2005;25:204-216. doi:10.1038/sj.jcbfm.9600020
63. Stanisz GJ, Odrobina EE, Pun J, et al. T1, T2 relaxation and magnetization transfer in tissue at 3T. *Magn Reson Med*. 2005;54:507-512. doi:10.1002/mrm.20605
64. Zhang X, Petersen ET, Ghariq E, et al. In vivo blood T1 measurements at 1.5 T, 3 T, and 7 T. *Magn Reson Med*. 2013;70:1082-1086. doi:10.1002/mrm.24550
65. Zhao JM, Clingman CS, Närväinen MJ, Kauppinen RA, Van Zijl PC. Oxygenation and hematocrit dependence of transverse relaxation rates of blood at 3T. *Magn Reson Med*. 2007;58:592-597. doi:10.1002/mrm.21342
66. Federau C, O'Brien K, Meuli R, Hagmann P, Maeder P. Measuring brain perfusion with intravoxel incoherent motion (IVIM): initial clinical experience. *J Magn Reson Imaging*. 2014;39:624-632. doi:10.1002/jmri.24195
67. Le Bihan D. What can we see with IVIM MRI? *Neuroimage*. 2018;187:1-12. doi:10.1016/j.neuroimage.2017.12.062
68. Liao YP, Urayama SI, Isa T, Fukuyama H. Optimal model mapping for intravoxel incoherent motion MRI. *Front Hum Neurosci*. 2021;15. doi:10.3389/fnhum.2021.617152
69. Palomares JA, Tummala S, Wang DJ, et al. Water exchange across the blood-brain barrier in obstructive sleep apnea: an MRI diffusion-weighted pseudo-continuous arterial spin labeling study. *J Neuroimaging*. 2015;25:900-905. doi:10.1111/jon.12288
70. Tang X, Cai F, Ding DX, Zhang LL, Cai XY, Fang Q. Magnetic resonance imaging relaxation time in Alzheimer's disease. *Brain Res Bull*. 2018;140:176-189. doi:10.1016/j.brainresbull.2018.05.004
71. Miller DH, Johnson G, Tofts PS, Macmanus D, McDonald WI. Precise relaxation time measurements of normal appearing white matter in inflammatory central nervous system disease. *Magn Reson Med*. 1989;11:331-336. doi:10.1002/mrm.1910110307
72. Papadopoulos K, Tozer DJ, Fisniku L, et al. T I-relaxation time changes over five years in relapsing-remitting multiple sclerosis. *Mult Scler*. 2010;16:427-433. doi:10.1177/1352458509359924
73. Gracien RM, Reitz SC, Hof SM, et al. Assessment of cortical damage in early multiple sclerosis with quantitative T2 relaxometry. *NMR Biomed*. 2016;29:444-450. doi:10.1002/nbm.3486
74. Wardlaw JM, Smith EE, Biessels GJ, et al. Neuroimaging standards for research into small vessel disease and its contribution to ageing and neurodegeneration. *Lancet Neurol*. 2013;12:822-838. doi:10.1016/S1474-4422(13)70124-8
75. Caunca MR, De Leon-Benedetti A, Latour L, Leigh R, Wright CB. Neuroimaging of cerebral small vessel disease and age-related cognitive changes. *Front Aging Neurosci*. 2019;11:1-15. doi:10.3389/fnagi.2019.00145
76. Brandhofe A, Stratmann C, Schüre JR, et al. T2 relaxation time of the normal-appearing white matter is related to the cognitive status in cerebral small vessel disease. *J Cereb Blood Flow Metab*. 2021;41:1767-1777. doi:10.1177/0271678X20972511
77. Draganski B, Ashburner J, Hutton C, et al. Regional specificity of MRI contrast parameter changes in normal ageing revealed by voxel-based quantification (VBQ). *Neuroimage*. 2011;55:1423-1434. doi:10.1016/j.neuroimage.2011.01.052
78. Callaghan MF, Freund P, Draganski B, et al. Widespread age-related differences in the human brain microstructure revealed by quantitative magnetic resonance imaging. *Neurobiol Aging*. 2014;35:1862-1872. doi:10.1016/j.neurobiolaging.2014.02.008
79. Knight MJ, McCann B, Tsivos D, Couthard E, Kauppinen RA. Quantitative T1 and T2 MRI signal characteristics in the human brain: different patterns of MR contrasts in normal ageing. *Magn Reson Mater Phys Biol Med*. 2016;29:833-842. doi:10.1007/s10334-016-0573-0
80. Lin Z, Lance E, McIntyre T, et al. Imaging blood-brain barrier permeability through MRI in pediatric sickle cell disease: a feasibility study. *J Magn Reson Imaging*. 2022;55:1551-1558. doi:10.1002/jmri.27965
81. Donahue MJ, Jan van Laar P, van Zijl PC, Stevens RD, Hendrikse J. Vascular space occupancy (VASO) cerebral blood volume-weighted MRI identifies hemodynamic impairment in patients with carotid artery disease. *J Magn Reson Imaging*. 2009;29:718-724. doi:10.1002/jmri.21667
82. Harrison IF, Siow B, Akilo AB, et al. Non-invasive imaging of CSF-mediated brain clearance pathways via assessment of perivascular fluid movement with diffusion tensor MRI. *Elife*. 2018;7:1-14. doi:10.7554/eLife.34028
83. Hirschler L, Aldea R, Petitclerc L, et al. High resolution T2-prepared MRI enables non-invasive assessment of CSF flow in perivascular spaces of the human brain. Paper presented at: Proceedings of the 27th Annual Meeting of ISMRM, Montreal, Quebec, Canada; 2019:0746.
84. Hladky SB, Barrand MA. Fluid and ion transfer across the blood-brain and blood-cerebrospinal fluid barriers; a comparative account of mechanisms and roles. *BioMed Central*. 2016;13. doi:10.1186/s12987-016-0040-3
85. Zeppenfeld DM, Simon M, Haswell JD, et al. Association of perivascular localization of aquaporin-4 with cognition and Alzheimer disease in aging brains. *JAMA Neurol*. 2017;74:91-99. doi:10.1001/jamaneurol.2016.4370
86. Lu H, Ge Y. Quantitative evaluation of oxygenation in venous vessels using T2-Relaxation-Under-Spin-Tagging MRI. *Magn Reson Med*. 2008;60:357-363. doi:10.1002/mrm.21627
87. Lu H, Xu F, Grgac K, Liu P, Qin Q, Van Zijl P. Calibration and validation of TRUST MRI for the estimation of cerebral blood oxygenation. *Magn Reson Med*. 2012;67:42-49. doi:10.1002/mrm.22970

SUPPORTING INFORMATION

Additional supporting information may be found in the online version of the article at the publisher's website.

Table S1. Model assumptions

15222594, 0, Downloaded from https://onlinelibrary.wiley.com/doi/10.1002/mrm.29616 by University College London UCL Library Services, Wiley Online Library on [21/03/2023]. See the Terms and Conditions (https://onlinelibrary.wiley.com/terms-and-conditions) on Wiley Online Library for rules of use; OA articles are governed by the applicable Creative Commons License

Figure S2. Assumption of infinite relaxation times with f_i^{eq} an additional free parameter in the 2CM model
Figure S3. Parameter distributions (variable SNR)
Figure S4. Dependence of D_i on relaxation times in the 2CM model
Figure S5. In vivo data
Figure S6. In vivo residuals
Figure S7. In vivo exchange rate maps (all subjects; regional fits)
Figure S8. In vivo parameter maps (single subject; voxel-wise fits)
Figure S9. Dependence of k_r on blood T_2 and oxygenation level
Section S10. Definition of blood volume

How to cite this article: Powell E, Ohene Y, Battiston M, Dickie BR, Parkes LM, Parker GJM. Blood-brain barrier water exchange measurements using FEXI: Impact of modeling paradigm and relaxation time effects. *Magn Reson Med*. 2023;1-17. doi: 10.1002/mrm.29616

APPENDIX A. EIGENVALUES AND EIGENVECTORS OF EXCHANGE-RELAXATION MATRIX EXPONENTIAL

The eigenvalues λ and eigenvectors $\boldsymbol{v}$ of the matrix $\boldsymbol{R}_1 + \boldsymbol{k}$ are given by:

$$\lambda_\pm = \frac{B \pm \sqrt{A}}{2}\ ; \quad v_\pm = \frac{2\left(R_{1,e} + k_{ei}\right) - (B \mp \sqrt{A})}{2k_{ie}}, \quad \text{(A1)}$$

where

$$A = \left(R_{1,e} - R_{1,i} + k_{ei} - k_{ie}\right)^2 + 4k_{ie}k_{ei} \quad \text{(A2)}$$

$$B = R_{1,e} + R_{1,i} + k_{ie} + k_{ei}. \quad \text{(A3)}$$

Elements of the matrix exponential $\boldsymbol{C} = e^{-(\boldsymbol{R}_1+\boldsymbol{K})t}$, computed as $\boldsymbol{C} = \boldsymbol{V}e^{\boldsymbol{\Lambda}}\boldsymbol{V}$ with $\boldsymbol{V}$ a matrix of eigenvectors and $\boldsymbol{\Lambda}$ a diagonal matrix of eigenvalues, are thus:

$$C_{1,1} = \frac{1}{2\sqrt{A}}\left[\left(R_{1,i} - R_{1,e} + \sqrt{A} - k_{ei} + k_{ie}\right)e^{-\frac{t_m}{2}(B+\sqrt{A})} - \left(R_{1,i} - R_{1,e} - \sqrt{A} - k_{ei} + k_{ie}\right)e^{-\frac{t_m}{2}(B-\sqrt{A})}\right], \quad \text{(A4)}$$

$$C_{1,2} = -\frac{k_{ei}}{\sqrt{A}}\left[e^{-\frac{t_m}{2}(B+\sqrt{A})} - e^{-\frac{t_m}{2}(B-\sqrt{A})}\right]. \quad \text{(A5)}$$

$$C_{2,1} = -\frac{k_{ie}}{\sqrt{A}}\left[e^{-\frac{t_m}{2}(B+\sqrt{A})} - e^{-\frac{t_m}{2}(B-\sqrt{A})}\right]. \quad \text{(A6)}$$

$$C_{2,2} = \frac{1}{2\sqrt{A}}\left[\left(R_{1,i} - R_{1,e} + \sqrt{A} - k_{ei} + k_{ie}\right)e^{-\frac{t_m}{2}(B-\sqrt{A})} - \left(R_{1,i} - R_{1,e} - \sqrt{A} - k_{ei} + k_{ie}\right)e^{-\frac{t_m}{2}(B+\sqrt{A})}\right]. \quad \text{(A7)}$$

15222594, 0, Downloaded from https://onlinelibrary.wiley.com/doi/10.1002/mrm.29616 by University College London UCL Library Services, Wiley Online Library on [21/03/2023]. See the Terms and Conditions (https://onlinelibrary.wiley.com/terms-and-conditions) on Wiley Online Library for rules of use; OA articles are governed by the applicable Creative Commons License